UNIVERSITY OF TARTU

Faculty of Science and Technology

Institute of Physics

Jaan Viru

# DESIGN AND TESTING OF ATTITUDE DETERMINATION SENSORS FOR ESTCUBE-1

Bachelor's Thesis

Supervisors: M.Sc. Andris Slavinskis

M.Sc. Riho Vendt

Tartu 2013

# Contents

# Acronyms and Abbreviations

**ADC**  Analog To Digital Converter

**ADCS**  Attitude Determination and Control System

**CDHS**  Command and Data Handling System

**COTS**  Commercial Off-the-Shelf

**COM**  Communications System

**E-sail**  Electric Solar Wind Sail

**EPS**  Electrical Power System

**GPS**  Global Positioning System

**I$^2$C**  Inter-Integrated Circuit

**LSB**  Least Significant Bit

**MCU**  microcontroller Unit

**MEMS**  Micro- Electro- Mechanical Systems

**MOEMS**  Micro- Opto- Electro- Mechanical System

**MUX**  Multiplexer

**SPI**  Serial Peripheral Interface

**RBF**  Remove Before Flight Pin

**PCB**  Printed Circuit Board

**UART**  Universal Asynchronous Receiver/Transmitter

# 1   Introduction

The CubeSat standard was developed in 1999 by California Polytechnic State University and Stanford University [1]. First CubeSats where mostly developed by universities. In recent years more companies have also developed interest in CubeSats due to low cost. The low cost of CubeSats allows companies such as Boeing [2] to experiment with new technologies and test different algorithms. Low cost of CubeSats also allows new countries and companies to enter space such as the Hungarian first satellite MaSat-1 [3].

The mission of the first Estonian satellite ESTCube-1 is to test new propulsion method, Electric Solar Wind Sail (E-sail) [4]. The experiment will be performed in polar low-Earth orbit at altitude of 670 km. ESTCube-1 will deploy a single 10 m long Heytether. Deployment is achieved by spinning the satellite and reeling out the tether with help of centrifugal force. [5]

ESTCube-1 Attitude Determination and Control System (ADCS) has due to innovative scientific mission considerably higher requirements than an average CubeSat mission. Main mission critical steps rely on ADCS. For centrifugal tether deployment the satellite is required to spin-up: reach angular speed around the satellite z-axis equal to ≈360 deg/s and align its spin axis with the Earth's polar axis with a pointing error less than 3 deg. Spin rate around x- and y-axes should be close to zero. ADCS sensors have to accurately measure attitude and rotation speed to control satellite maneuvers and detect electric solar sail effect.

This thesis describes the ESTCube-1 ADCS hardware design. The designing process and development of ADCS main board is one of the main subjects. The second part will describe testing and calibration process of magnetometer and gyroscope. Final section of discussion and conclusions will talk about recommendations for future projects. This thesis does not include development and calibration of sun sensors which is described in other thesis [6]. Development of coils and software design are also not included in this thesis.The objectives of this work are stated as follows:

- Design ADCS main board.

- Calibrate and find the uncertainty of the ADCS sensors.

Importance of this thesis is development, testing and calibrating of the Estonian first satellite ESTCube-1 ADCS main board. Analyzing the results, describing the problems encountered will increase further hardware projects quality.

# 2 Design of Attitude Determination and Control System

## 2.1 Overview of Previous Work

Previous research on small satellite ADCS has mainly focused on design description, choosing suitable sensors and actuators for the satellite. Multiple CubeSats ADCSs have their own microcontroller Unit (MCU) such as Compass-1 [7]. An ADCS with five Micro- Opto- Electro- Mechanical System (MOEMS) analog two-axis slit sun sensors and three-axis magnetometer composed of one and two-axis magnetometer HMC 1021/1022 is described. For active three-axis attitude control electromagnetic coils and coil drivers are used. ADCS has been designed on one four layer Printed Circuit Board (PCB) with dimensions of 75 mm x 80 mm. After the launch multiple mistakes were found such as angular misalignment of magnetic field reference vector and inaccurate calibration of sun sensor threshold values which made attitude determination impossible. [8]

On Cute-1.7+ADP II launched in 2008 similar setup is used [9]. Attitude is measured with two sun sensors based on incident angle sensors Hamamatsu S6560, on each of five sides. To measure magnetic field Honywell HMR2300 was put on external PCB. HMR2300 is made from one- and two-axial analog sensors HMC1001, HMC1002, Analog To Digital Converter (ADC) and digital interface RS-232 or RS-485. In comparison with Compass-1 analog gyroscope ADXRS150 was added. For three-axis attitude control magnetic torquers are used. To improve ADCS performance, output torque of the actuators has been tripled compared with Cute - 1.7 + ADP I. ADCS of Cute - 1.7 + ADP II was successful.

HAUSAT-2 is a 30 kg nanosatellite, developed by graduate students from Space System Research Laboratory. Pitch bias momentum method for 3-axis stabilization is used. Pitch bias momentum method enables control in the roll and yaw directions by pointing the rotational axis of the momentum wheel that has angular momentum in the pitch direction of the satellite. One momentum wheel in pitch axis, 3-axis magnet torquers, 2-axis sun sensors, a 3-axis magnetometer and a star tracker are used for attitude estimation. HAUSAT-2 should be launched in May 2013. [10], [11]

In 2008 CanX-2 was launched with main mission to test technologies for formation flight.

CanX-2 ADCS is equipped with Cold-gas propulsion system, a 30 mN · m · s nanosatellite reaction wheel as a part of a three-axis stabilized Y thomson-configuration attitude control subsystem, and a commercially available Global Positioning System (GPS). Attitude determination accuracy of ±1.5 deg is achieved with six sun sensors and a magnetometer, developed by University of Toronto Institute for Aerospace Studies Space Flight Laboratory. Magnetometer is deployed 20 cm from the satellite. The satellite mission was successful and all main mission objectives were fulfilled. In the beginning of mission accuracy of attitude estimation error was 1.5 deg but in two years it had degraded to 2 deg. Problems only arose with higher-than-expected albedo influence on sun sensors. [12]

On CubeSat UWE-1, active attitude control was not used [13]. Attitude was controlled passively, with permanent magnets on two axes. The axis without permanent magnet was selected as spin axis. The satellite was functional under a month.

## 2.2   Requirements

Requirements for the hardware of ADCS stated as follows:

- Determine the rotation of spacecraft and measure change in angular speed caused by E-sail effect.

- Stop tumbling.

- Reach angular speed around the satellite z-axis equal to ≈360 deg/s.

- Command and Data Handling System (CDHS) microcontroller shall be used for ADCS

- Mass limit of 100 g.

- Electrical Power System (EPS) hardware power limit on ADCS main board is 500 mW.

- Mission duration of one year.

## 2.3   Overall Description of the Hardware

ADCS hardware design is driven by environmental conditions in space and MCU on CDHS. Due to ESTCube-1 general design philosophy, Commercial Off-the-Shelf (COTS) components

were preferred in the design. Modern COTS components have higher performance per volume ratio than typical aerospace products at the cost of insignificant loss of reliability .

Sensor duplication has been implemented to increase robustness. In order to mitigate the risk of mission failure due to sensor damage, redundant serial peripheral interface bus (SPI) and inter-integrated circuit ($I^2C$) lines are also in use. Most of the unconnected pins are connected to the ground to avoid charge build-up. Filters are applied where possible to decrease noise level. For sun sensor inputs filters are particularly important because of the long wires which capture noise between ADCS and sun sensor PCBs. Twisted pairs of signal and ground are also used on connection with sun sensor to reduce noise further. For more accurate voltage measurements external charge pump and voltage reference were added to provide ADC more stable and accurate reference.
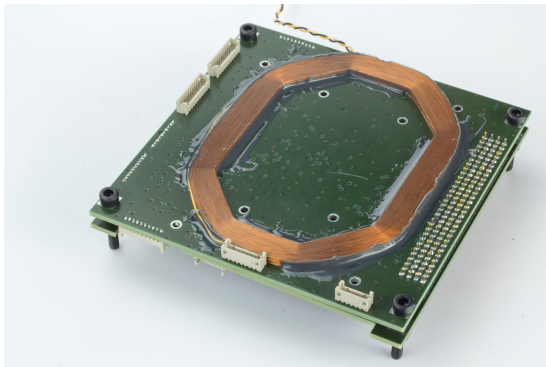


Figure 1: ADCS/CDHS from ADCS side, top side



Figure 2: ADCS/CDHS from CDHS side, bottom side

In order to ensure low resistance between ground planes, free regions of the PCB are covered with through-hole vias. Ground vias are placed as close to sensors' ground pads as possible to reduce ground resistance even more. Structural connection points with CDHS are also grounded and thus CDHS and ADCS have smaller resistance to provide more error free communication between subsystems. Top layer has been filled with a ground plane to shield electronics from currents induced by the coil which is mended a the top of the board.

Due to location of ADCS (see Appendix A), connections of Remove Before Flight Pin (RBF) and access port with CDHS, EPS and Communications System (COM) have to go through ADCS. Due to volume constraints, the vertical gap between ADCS and CDHS has been minimized. All the connectors have been moved to the edges. See Figures 1,2 for an illustration. Figure 3 describes ADCS interfaces with CDHS, EPS and sensor redundancy.
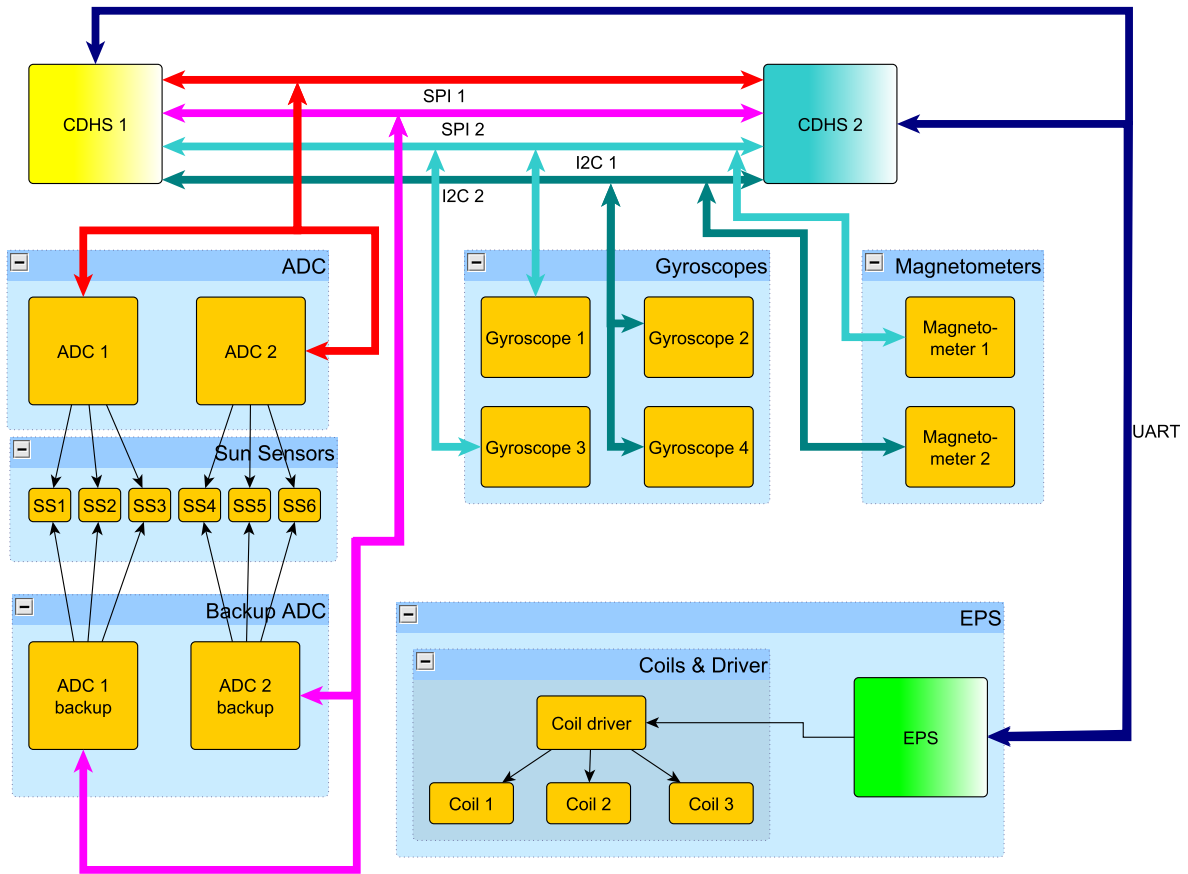
Figure 3: ADCS interfaces. SS1-SS6 are sun sensor analog inputs.

## 2.4   Magnetometer

ADCS contains two three-axes magnetometers which measure local magnetic field vector. Coils are driven based on magnetic field measurements. Magnetic field measurements are used for attitude estimations as well. Sensors included in initial trade study were Honeywell HMC5843, HMC1043, HMC1053, HMR3400 and PNI MicroMag3. HMC5843 [14] was chosen because of its low mass, low power consumption and sufficient resolution. When HMC5843 was discontinued, a similar sensor Honeywell HMC5883L [15] was chosen. HMC5883L stands out with parameters listed in Table 1.

On ADCS main board two magnetometers HMC5883L are used to mitigate the risk of mission failure due to sensor damage. Magnetometer itself can withstand maximum of 3.6 V potential difference between inputs and ground. Due to main bus connection limitations, EPS only supplies ADCS with 5 V bus, low-dropout linear regulator LM1117IMP-3.3/NOBP by National Semiconductor is used for voltage level down converting to 3.3 V. Low-dropout linear regulator

Table 1: Parameters of magnetometer HMC5883L

| Parameter | Value | Unit |
|---|---|---|
| Range | $\pm 1.3$ | G |
| Resolution | 5 | mG |
| Heading accuracy | 2 | deg |
| Sampling resolution | 12 | bits |
| Dimensions | $3.0 \times 3.0 \times 0.9$ | mm |
| Max output rate | 160 | Hz |
| Average power consumption | 100 | $\mu$A |
| Operating temperature | -35 to 85 | °C |

is used because current drawn on 3.3 V bus is low (40 mA). Multiple capacitors of different capacitance in output and input circuit are used to stabilize the output voltage.

Magnetometer HMC5883L contains three magnetoresistive sensors. The sensor is made of a nickel-iron thin-film. Presence of magnetic field causes the change of voltage. After converting results to digital values, results can be read out on I²C bus. No more than one magnetometer can be present on a single I²C bus without I²C switch or Multiplexer (MUX) because HMC5883L does not offer address configuration capabilities.

## 2.5 Gyroscope

ESTCube-1 attitude determination system contains four three-axes gyroscopic sensors which measure satellite angular speed. The sensors included in initial market research were Invensense ITG-3200, IDG-500, IXZ-500 and STMicroelectronics LYPR540AH, LPR510AL, LPY510AL. Invensense ITG-3200 and STMicroelectronics LYPR540AH stand out in almost all considered categories: size, range, resolution and the most importantly, those are the only sensors with three axes. Invensense ITG-3200 [16] was chosen because of lower power consumption and parameters listed in Table 2.

ADCS main board consists of 4 gyroscopes which are rotated 90 deg in respect to each other, to filter out uncertainties and improve accuracy of angular speed measurements. Rotated gyroscopic sensors are particularly effective to filter out temperature and cross-axis uncertainty.

Table 2: Parameters of gyroscope ITG-3200

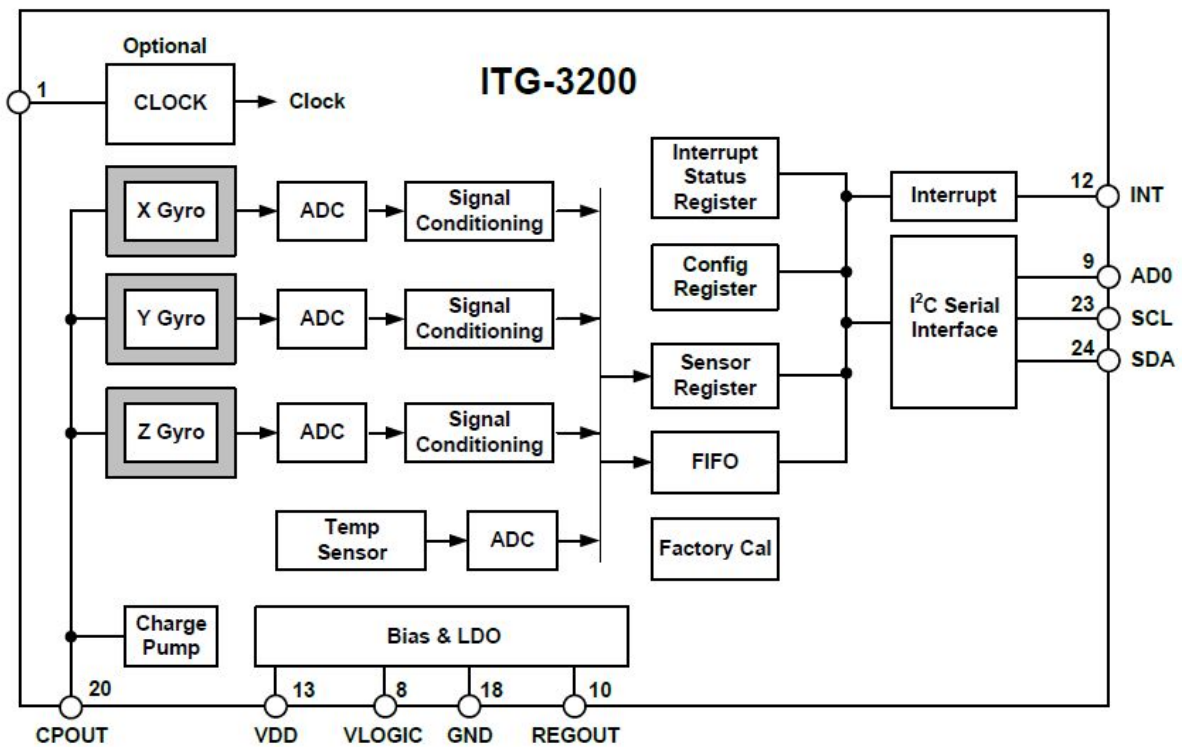| Parameter | Value | Unit |
|---|---|---|
| Range | +/- 2000 | °/sec |
| Sensitivity | 14.375 | LSBs per °/sec |
| Operating temperature | -40 to 105 | °C |
| Sampling resolution | 16 | bits |
| Normal Operating Current | 6.5 | mA |
| Max sample rate | 8 | kHz |
| QFN package | $4 \times 4 \times 0.9$ | mm |
| Axes | 3 | |



Figure 4: ITG-3200 block diagram [16]

Number of connections between gyroscopes and CDHS has been minimized due to limited pins in the main connector. To optimize number of connections interrupt digital output pin has not been used, which notifies the user if new data is available. I$^2$C slave address least significant bit (LSB) pin on two gyroscopes have been pulled down and on other two pulled up, to ensure different device addresses. This allows putting two gyros on same I$^2$C line. Same power supply

with magnetometer is used for communication on 3.3 V tolerant I²C bus.

The accuracy of ITG-3200 is mainly defined by three Micro-Electro-Mechanical Systems (MEMS) rate gyroscopes and ADC as shown in Figure 4. MEMS gyroscopes such as ITG-3200 use the Coriolis Effect to measure angular speed. In most MEMS vibratory gyroscopes the sensitive element can be represented as suspended mass supported by elastic suspension elements [17], [18].

## 2.6 Analog to Digital Converter

ADCS subsystem has 26 analog inputs. Sun sensors require 24 analog inputs, leaving two for temperature sensors KTY82-110. There are four ADCs on two SPI buses on ADCS. In phase B ADS1158 was considered. In the beginning of phase C MAX1230 [19] was chosen. The reasons are the following: smaller number of pins, more testing done due to its use in EPS and the parameters listed in Table 3.

Table 3: Parameters of ADC MAX1230 and ADS1158

| Parameter | MAX1230 | ADS1158 | Unit |
|---|---|---|---|
| Channels | 16 | 16 | |
| Total number of pads | 24 | 48 | |
| Sampling resolution | 12 | 16 | bits |
| Max Sampling rate | 300 | 125 | ksps |
| Dimensions | $5.84 \times 8.56 \times 1.55$ | $7.10 \times 7.10 \times 0.90$ | mm |
| Packet | QSOP | QFN | |
| Operating temperature range | -40 to 80 | -40 to 105 | deg /s |
| Interface | 3-Wire SPI | 3-Wire SPI | |

Due to ADC internal reference voltage inaccuracy and dependence on temperature, external reference voltage circuit was designed. Reference voltage circuit contains charge pump MCP1252 and reference voltage ADR3450ARJZ, which outputs exactly 5 V. The charge pump is added to design due to the fact that input voltage of ADR3450ARJZ has to be higher than output voltage all times.

To lower one Serial Peripheral Interface (SPI) bus voltage from 5 V to 3.3 V level converter TXB0108-SOP has been inserted between CDHS MCU and ADCs. Only on one bus level conversion is implemented because the second SPI bus is 5 V tolerant from the side of CDHS. Functional diagram of MAX1230 is in Figure 5
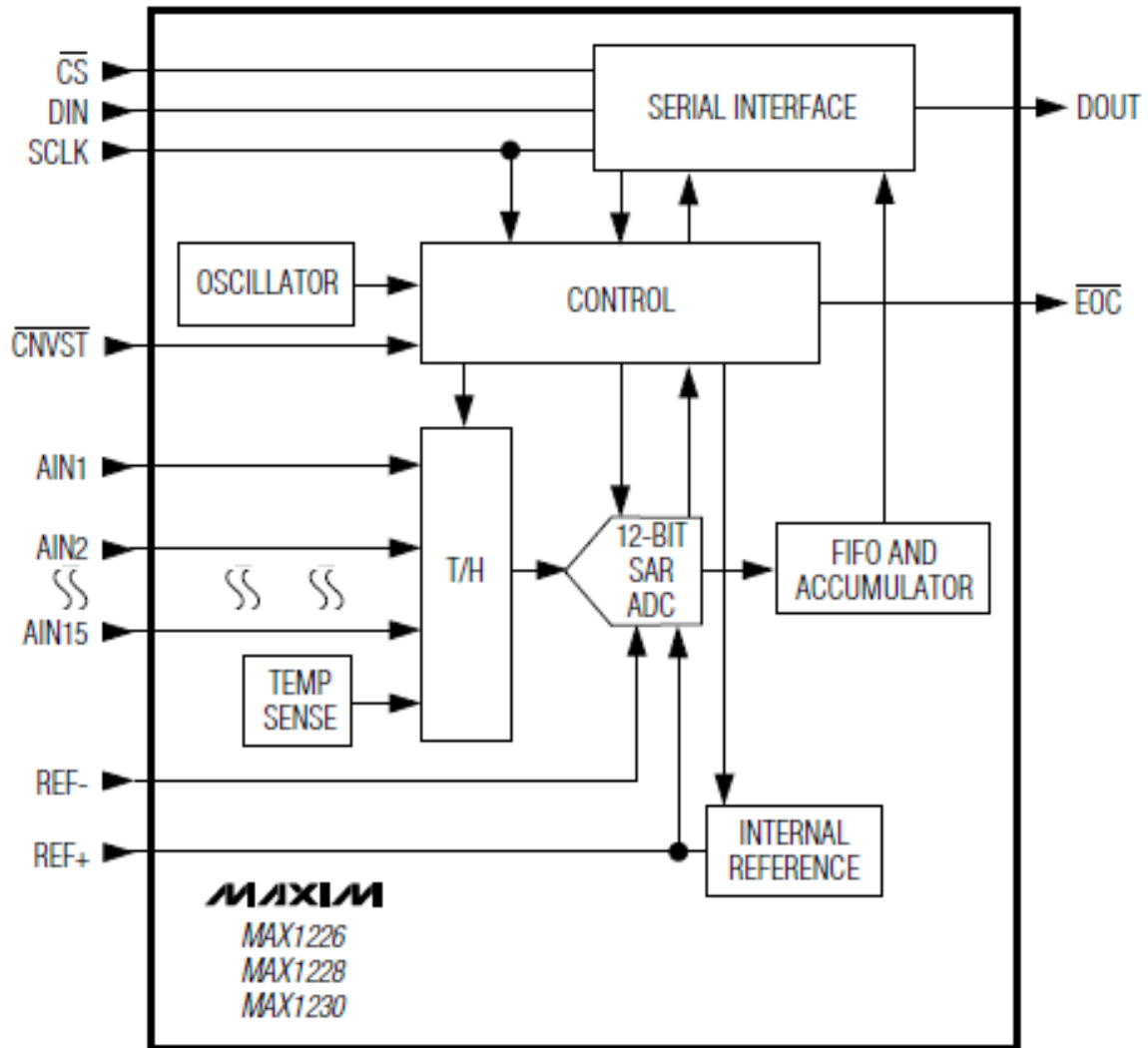
Figure 5: MAX1230 functional diagram [19]

In order to measure ADCS board temperature, both ADC internal temperature sensors and external sensors are used. Temperature sensors of gyroscopes are not used due to their inaccuracy.

## 2.7 Schematics and Layout

The schematics of final design are presented in Appendix C. The final PCB design layout is shown in Appendix D. ADCS can fully function only when connected with CDHS board. ADCS/CDHS debug board is needed to connect ADCS with computer for data transfer and power supply without EPS.

# 3 Testing and Calibration of Gyroscope

## 3.1 Overview of Work

Magnetometer and gyroscope calibration and uncertainty measurement process will be described in next two paragraphs. Calibration is performed to increase the accuracy of measurements. ESTCube-1 ADCS uses unscented Kalman filter for attitude estimation [20] that is improved with uncertainty budgets of magnetometer and gyroscope. Measurement calculations are done accordingly with Expression of the Uncertainty of Measurement in Calibration [21].

For example, triple CubeSat Radio Aura Explorer (RAX) all ADCS sensors were calibrated pre-flight to determine sensor characteristics such as bias and accuracy. Ideal Aerospace Model 1270VS rate table was used to perform gyroscope calibration. Due to expected deployment dynamics RAX ADCS was spun up to $\pm$ 60 deg/s. Magnetometer calibration pre-flight was done with two configurations. First, stand-alone magnetometers were calibrated between Helmholtz cage. Secondly, magnetometers were tested after satellite integration. Additionally, extended calibration will be performed on orbit. [22] Similar approach was used by author for ESTCube-1 ADCS testing.

## 3.2 Calibration of Gyroscopes

Calibration of gyroscope is performed to find calibration function to convert gyroscopes measurements from arbitrary units to angular speed in rad/s. Calibration function is estimated for x-, y-and z-axes. During the calibration, two types of values are measured. First, the output impulse frequency of Photodiode GP2S30 is measured with oscilloscope RTO 1014 [23], [24]. Frequency of photodiode is proportional to the angular speed of rotating bench. Due to mechanical gear photodiode registers rotating bench angular speed 17 times faster. Second, the gyroscope digital register is read two times per second. To transfer ADCS data to computer, wireless Universal Asynchronous Receiver/Transmitter (UART) communication module from XBEE is used. Setup is shown in Figure 6.

For calibrating z-axis, 5 sets of 20 gyroscope readings are taken for each of 8 different speed in clockwise and 8 different speeds anticlockwise. During x- and y-axes calibration, number of different speeds were reduced two times due to relation linearity which was discovered calibrating z-axis. Measurements are taken from 2 rad/s to 10 rad/s clock- and anticlockwise with
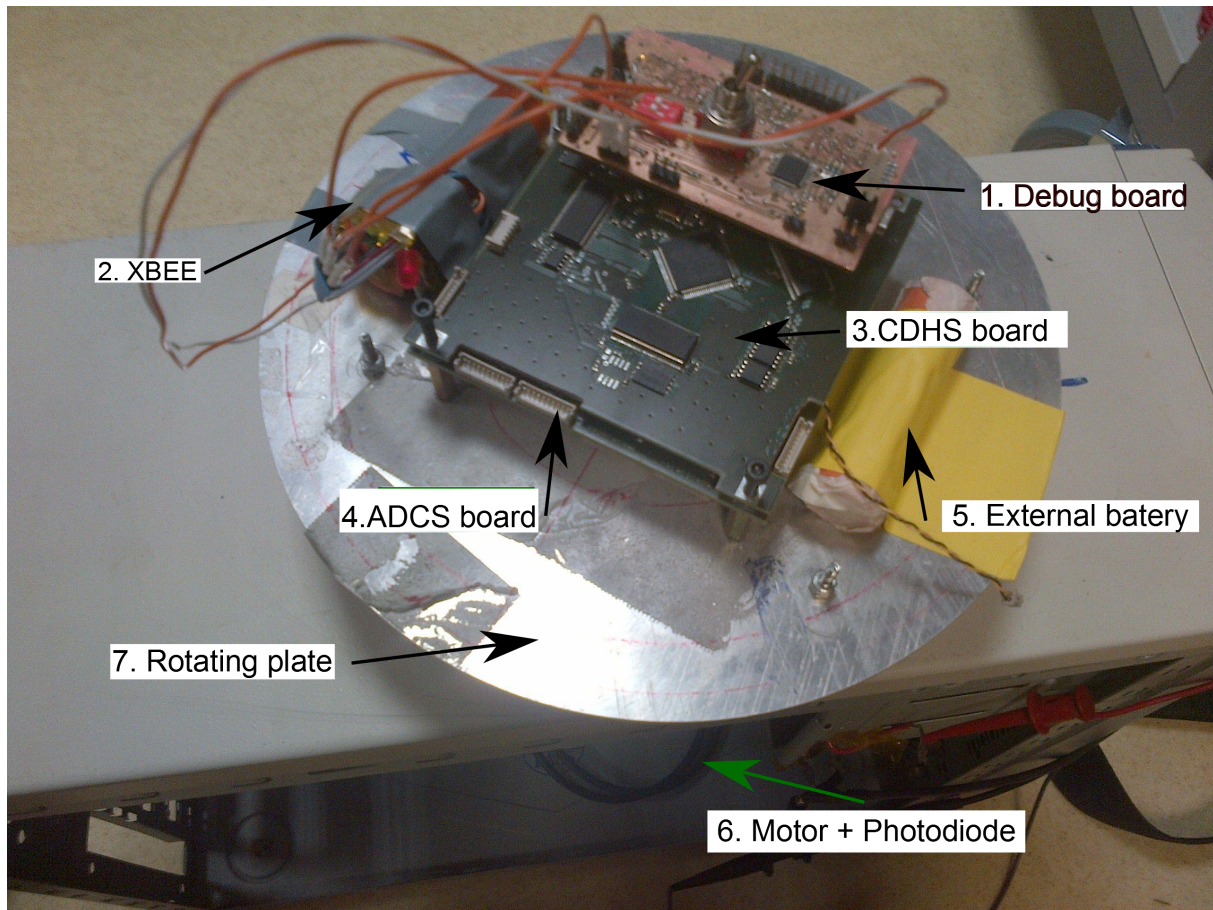
Figure 6: Calibration setup of the gyroscopes

equal steps. ESTCube-1 maximum angular speed estimations and rotation bench limitations were taken into account to decide speed boundaries. Multiple tests were performed to measure sensor results while no rotation occurs. Stand still measurements are required to calculate zero bias. Finally, angular speed measured with oscilloscope is compared with gyroscopic sensor readings. Gyroscope calibration curve, cross-axis interference and uncertainties of gyroscope readings are calculated from the received data.

In Figure 7 calibration curve of gyroscope z-axis readings in arbitrary units and angular speed in rad/s is found. Standard deviation of each measurement set is plotted as error bar on that figure. Calibration curves of x-and y-axis are similar. Equation 1 describes calibration functions of gyroscope different axes, where $\omega_x$, $\omega_y$, $\omega_z$ are angular speeds around x-, y-and z-axes in rad/s and $r_x$, $r_y$, $r_z$ are gyroscope readings of x-, y-and z-axes in arbitrary units.
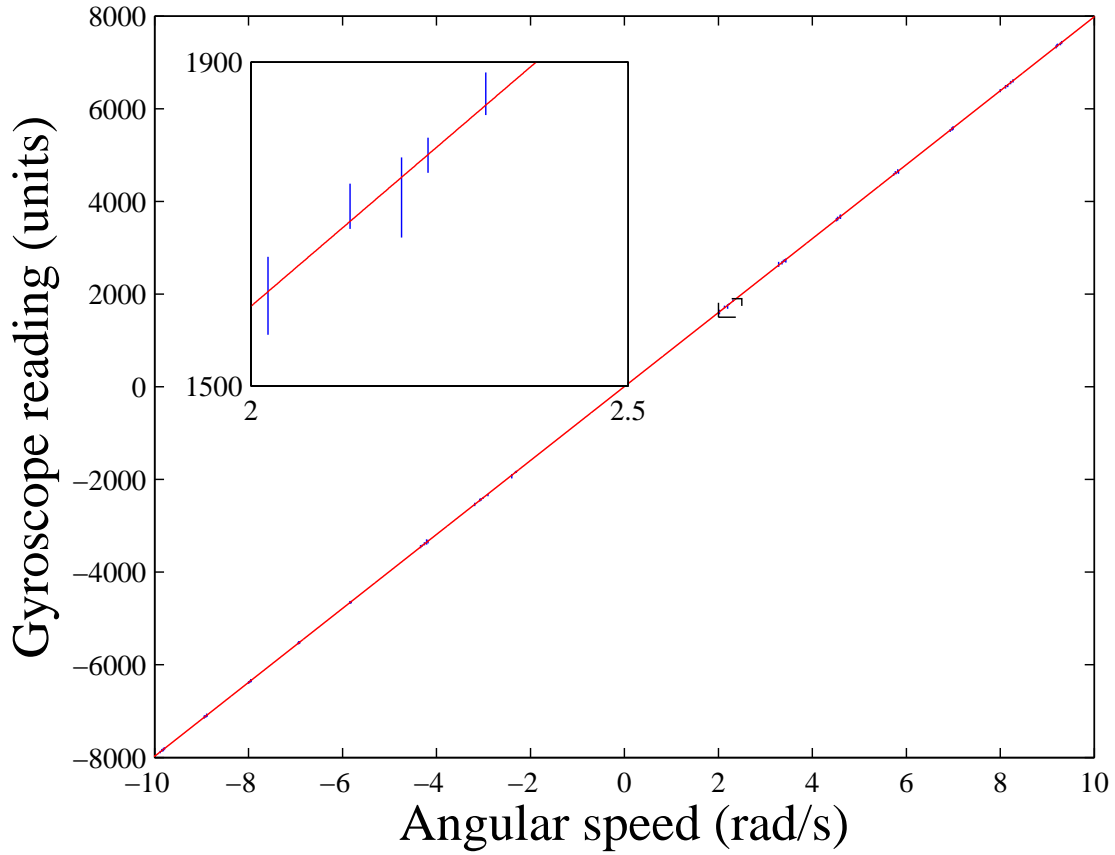
15

Figure 7: Calibration curve of z-axis with gyroscope reading standard deviation. Inline frame is zoomed in sections in section showing the dispersion of single point measurement series.

$$\omega_x = \frac{r_x - 2.2}{799.7} \frac{\text{rad}}{\text{s}} \tag{1a}$$

$$\omega_y = \frac{r_y - 2.6}{800.5} \frac{\text{rad}}{\text{s}} \tag{1b}$$

$$\omega_z = \frac{r_z - 2.2}{798.0} \frac{\text{rad}}{\text{s}} \tag{1c}$$

The largest standard deviation of gyroscope reading is chosen to describe standard deviation of gyroscope reading. The calibration function which generates the largest uncertainty values is chosen without constant, to convert arbitrary units to rad/s in Equation 2, 3. B-type uncertainty of gyroscope reading is in Equation 4.

If $s$ is the highest standard deviation, $c$ is the chosen calibration function, $rtg$ is radians to degrees conversion constant and $n$ is number of measurements, then formula for gyroscope

reading standard deviation $\sigma\omega_S$ and gyroscope reading standard uncertainty $\delta\omega_S$ are

$$\sigma\omega_S = s \cdot c \cdot rtg$$

$$= 57.7 \text{ units} \cdot \frac{1}{798.0} \frac{\text{rad}}{\text{s} \cdot \text{unit}} \cdot \frac{360}{2 \cdot \pi} \frac{\text{deg}}{\text{rad}} = 4.1 \frac{\text{deg}}{\text{s}} \tag{2}$$

$$\delta\omega_S = \frac{\sigma\omega_S \frac{\text{deg}}{\text{s}}}{\sqrt{n}} = \frac{4.1 \frac{\text{deg}}{\text{s}}}{\sqrt{20}} = 0.9 \frac{\text{deg}}{\text{s}} \tag{3}$$

If $res$ is the resolution of the gyroscope, then gyroscope reading B-type uncertainty is

$$\delta\omega_B = \frac{res \frac{\text{deg}}{\text{s}}}{\sqrt{12}} = \frac{\pm 2000 \frac{\text{deg}}{\text{s}}}{\frac{2^{16}}{\sqrt{12}}}$$

$$= 0.02 \frac{\text{deg}}{\text{s}} \tag{4}$$

## 3.3 Uncertainty from Instability of Rotation Bench

The purpose of this test is to determine angular speed standard deviation. Test is conducted at angular speed of 2.8 rad/s, 6.0 rad/s and 9.3 rad/s. Test setup is the same as in angular speed test. Over 140 photodiode impulses are taken in each speed. For calculating rotation speed instability Formulas 5, 6 are used.

If $n$ is the number of measurements, $x_i$ is the measurement number $i$ and the mean value is $\bar{x}$, then a formula for calculating standard deviation $s$ is

$$s = \left(\frac{1}{n-1} \sum_{i=1}^{n} (x_i - \bar{x})^2\right)^{\frac{1}{2}} \tag{5}$$

The highest standard deviation from Table 4 is chosen to describe the instability of the rotation bench speeds.

Table 4: Rotation bench standard deviation

| Test Nr. | Speed (rad/s) | STD (rad/s) |
|----------|---------------|-------------|
| 1        | 2.8           | 0.006       |
| 2        | 6.0           | 0.012       |
| 3        | 9.3           | 0.019       |

If $\sigma\omega_R$ is the largest standard deviation and $n$ is number of measurements, then instability of

rotation bench $\delta\omega_R$ is

$$\sigma\omega_R = 0.019 \, \frac{\text{rad}}{\text{s}} \cdot \frac{360}{2 \cdot \pi} \frac{\text{deg}}{\text{rad}} = 1.1 \, \frac{\text{deg}}{\text{s}}$$

$$\delta\omega_R = \frac{\sigma\omega_R \frac{\text{deg}}{\text{s}}}{\sqrt{n}} = \frac{1.1 \frac{\text{deg}}{\text{s}}}{\sqrt{140}}$$

$$= 0.1 \, \frac{\text{deg}}{\text{s}} \tag{6}$$

## 3.4 Uncertainty from Signal Measurement Equipment

In this paragraph, oscilloscope frequency measurement B-type uncertainty is estimated. In gyroscope calibration oscilloscope Rohde & Schwarz RTO1014 is used. Equation 7 estimates the oscilloscope delta time accuracy [24]. Delta time accuracy describes the time measurement accuracy. Frequency variation due to delta time inaccuracy is calculated in Equation 9 to estimate oscilloscope uncertainty in Equation 8.

If $K$ is device constant specific to RTO1014, $R_S$ is real time sampling rate, $T_A$ is time base accuracy and $R$ is time reading, then delta time accuracy $\Delta t$ is

$$\Delta t = \pm(\frac{K}{R_S} + T_A \cdot |R|)$$

$$= \pm(\frac{0.18}{250000} \, \text{s} + \frac{5}{1000000} \cdot \frac{1}{6} \, \text{s}) = \pm 1.55 \cdot 10^{-6} \, \text{s} \tag{7}$$

If $|f_1 - f_2|$ is the frequency variation due to delta time inaccuracy, $\Delta t$ is delta time accuracy and $\omega$ represents maximum angular speed of angular speed test, then formula for oscilloscope uncertainty $uO$ is

$$u\omega_O = \frac{|f_1 - f_2| \cdot 360 \, \text{deg}}{\sqrt{12}}$$

$$= 5.1 \cdot 10^{-4} \, \frac{\text{deg}}{\text{s}} \tag{8}$$

were

$$f = \frac{\frac{\omega}{2 \cdot \pi}}{1 \pm \Delta t} \tag{9a}$$

$$f_1 = \frac{10/2 \cdot \pi}{1 - 1.55 \cdot 10^{-6}} \, \text{Hz} \tag{9b}$$

$$f_2 = \frac{10/2 \cdot \pi}{1 + 1.55 \cdot 10^{-6}} \, \text{Hz} \tag{9c}$$

## 3.5 Uncertainty from Cross Axis Interference

Calibration of gyroscope data is used to estimate how rotation in one axis affects two other axes. One axis rotation influence on other two axes is described on Figures 8, 9, 10, 11, 12, 13.
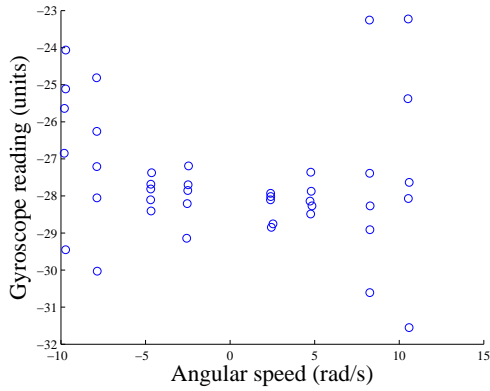


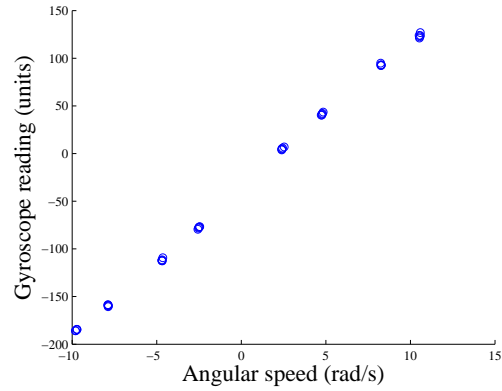Figure 8: Gyroscope Y-axis calibration while rotating around X-axis



Figure 9: Gyroscope Z-axis calibration while rotating around X-axis
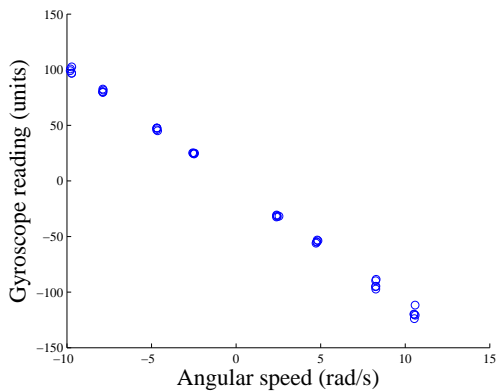


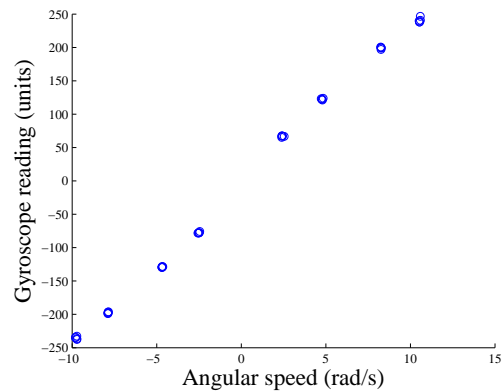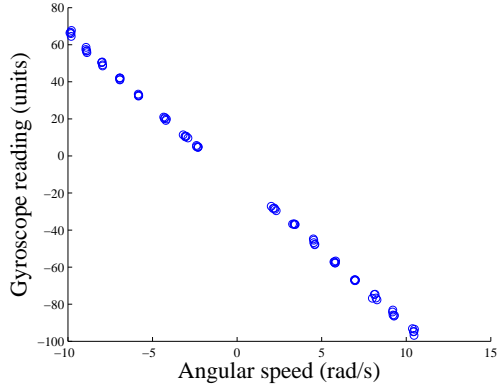Figure 10: Gyroscope X-axis calibration while rotating around Y-axis



Figure 11: Gyroscope Z-axis calibration while rotating around Y-axis

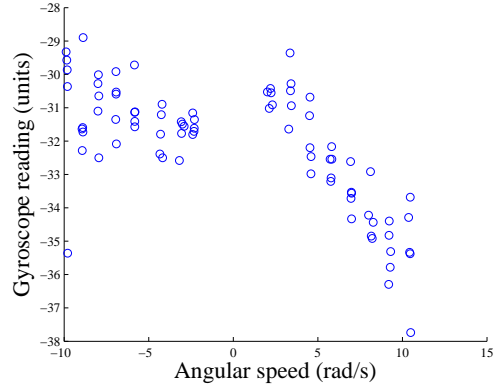Figure 12: Gyroscope X-axis calibration while rotating around Z-axis



Figure 13: Gyroscope Y-axis calibration while rotating around Z-axis

The biggest influence to one axis is chosen to describe uncertainty from the cross axis signal influence. To decrease uncertainty, boundaries are narrowed to -6.3 rad/s to 6.3 rad/s due to the mission parameters. The highest speed of 6.3 rad/s is achieved during the spin up. Equations 10, 11 estimate cross axis uncertainty.

If $\omega_{C,\,max_x}$ and $\omega_{C,\,min_x}$ are gyroscope reading maximum and minimum values in units from Figure 9, $\omega_{C,\,max_y}$ and $\omega_{C,\,min_y}$ are respectively gyroscope reading maximum and minimum values in units from Figure 11, defined angular speed boundaries and units to deg/s conversion from Equation 2 are implemented, then Formulas 10, 11 for estimating cross-axis uncertainty in units and deg/s are

$$\delta\omega_C = \sqrt{(\frac{|\omega_{C,\,max_x} - \omega_{C,\,min_x}|}{\sqrt{12}})^2 + (\frac{|\omega_{C,\,max_y} - \omega_{C,\,min_y}|}{\sqrt{12}})^2}$$

$$= \sqrt{(\frac{|70.8 \text{ units} + 134 \text{ units}|}{\sqrt{12}})^2 + (\frac{|158 \text{ units} + 148 \text{ units}|}{\sqrt{12}})^2}$$

$$= 106.2 \text{ units} \tag{10}$$

$$= 106.2 \text{ units} \cdot \frac{1}{798} \frac{\text{rad}}{\text{s} \cdot \text{unit}} \cdot \frac{360}{2 \cdot \pi} \frac{\text{deg}}{\text{rad}} = 7.6 \frac{\text{deg}}{\text{s}} \tag{11}$$

## 3.6 Effect of Temperature on Zero Speed Offset

The purpose of this test is to find zero speed bias dependency on temperature. Test is performed with thermal chamber VMT 04/16 at the temperature from -40 °C to 80 °C, with steps of 20 °C. Temperature chamber internal temperature sensor is used to measured temperature. Gyroscope

zero bias measurements are logged into a computer. To avoid interference with system under test, temperature chamber was not opened during the test. Different temperature influences on bias are shown on Figure 14.
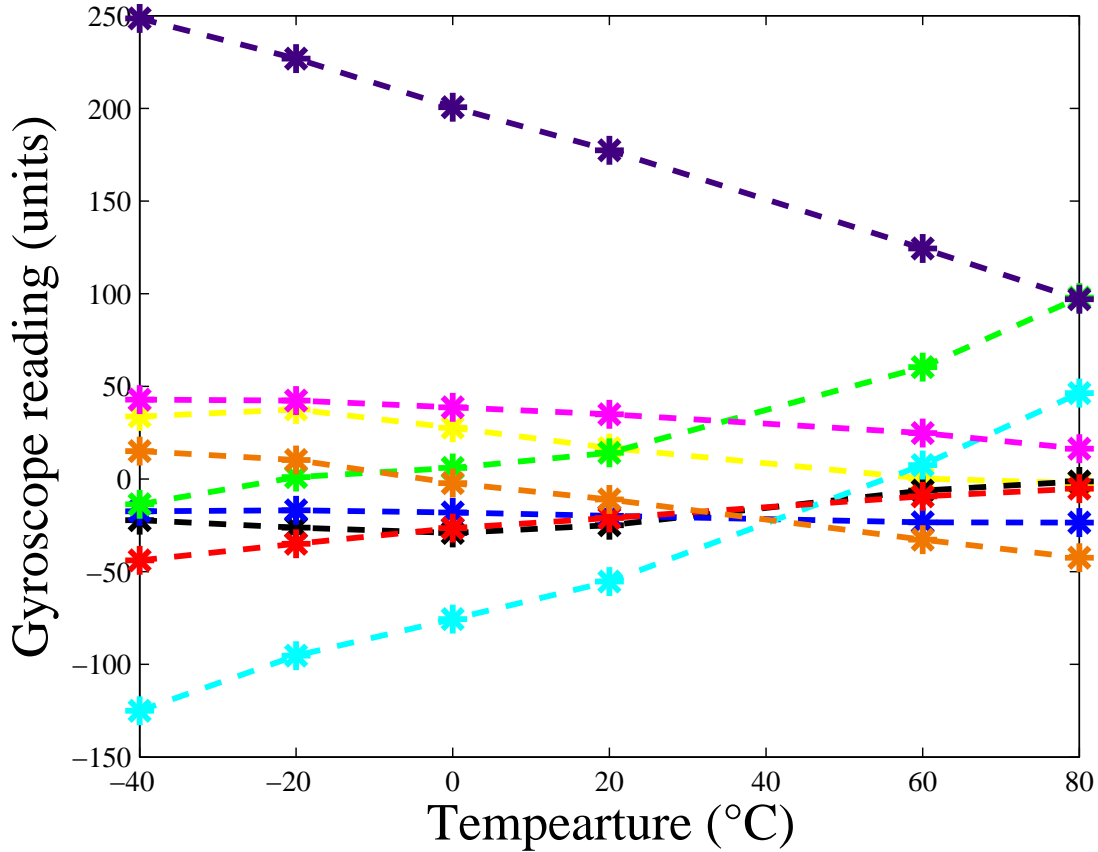


Figure 14: Dependency of zero offset on temperature. Yellow, black and blue lines are gyroscope zero x-, y-and z-axes; green, light blue and red lines are gyroscope one x-, y-and z-axes; pink, purple and orange lines are gyroscope three x-, y-and z-axes. Dots represent five measurement average

Compass-1 flight results on a similar orbit have shown that environment temperatures within satellite do not exceed -10 °C to 35 °C [8]. For this reason boundaries have been selected to be the same. Axis with the biggest temperature influence is chosen to estimate zero bias temperature drift in Equation 12.

If $\omega_{t,\,max}$ and $\omega_{t,\,min}$ are the gyroscope 1 y axis values at 35 and -10 and units to deg/s conversion

from Equation 2 is implemented, then zero location temperature drift uncertainty $\delta\omega_T$ is

$$\delta\omega_T = \frac{|\omega_{t,\,max} - \omega_{t,\,min}|}{\sqrt{12}} \cdot \frac{1}{798} \frac{\text{rad}}{\text{s} \cdot \text{unit}} \cdot \frac{360}{2 \cdot \pi} \frac{\text{deg}}{\text{rad}}$$

$$= 1.5 \frac{\text{deg}}{\text{s}} \tag{12}$$

## 3.7 Test in Vacuum

Test in vacuum is performed to determine sensor ability to survive vacuum environment and investigate vacuum influence on gyroscope reading zero bias. During tests device under test was not moved or rotated. Two tests were performed. First test was performed with normal atmospheric pressure 760 mmHg in vacuum chamber. Second test is performed in vacuum of $35 \cdot 10^{-2}$ mmHg. Finally results were compared to see the pressure effect on sensors. In Table 5 describes gyroscope one reading zero bias change with pressure in arbitrary units. Other gyroscopes have similar biases and are not shown in this table. The biggest zero speed bias change is used to estimate zero bias uncertainty in vacuum in Equation 13.

Table 5: Gyroscope reading zero bias change with pressure

| Axes | Measurement at pressure of $35 \cdot 10^{-2}$ mmHg | Measurement at pressure of 760 mmHg |
|------|---------------------------------------------------|-------------------------------------|
| x-axis | 3.4 units | 15.1 units |
| y-axis | -29.0 units | -24.4 units |
| z-axis | -28.5 units | -22.9 units |

If $|\omega_{V,\,max} - \omega_{V,\,min}|$ is the biggest zero bias change in units with pressure and Equation 2 is used for arbitrary units to deg/s conversion, then zero bias uncertainty due to vacuum $\delta\omega_V$ is

$$\delta\omega_V = \frac{|\omega_{V,\,max} - \omega_{V,\,min}|}{\sqrt{12}} \cdot \frac{1}{798} \frac{\text{rad}}{\text{s} \cdot \text{unit}} \cdot \frac{360}{2 \cdot \pi} \frac{\text{deg}}{\text{rad}}$$

$$= 3.3 \; units \cdot \frac{1}{798} \frac{\text{rad}}{\text{s} \cdot \text{unit}} \cdot \frac{360}{2 \cdot \pi} \frac{\text{deg}}{\text{rad}}$$

$$= 0.2 \frac{\text{deg}}{\text{s}} \tag{13}$$

## 3.8 Uncertainty Budget for Angular Speed

This budget describes angular speed calibration uncertainty.

- $\delta\omega_T$ - zero bias drift due to temperature

- $\delta\omega_R$ - instability of rotation bench

- $u\omega_O$ - oscilloscope uncertainty

- $\delta\omega_V$ - uncertainty of vacuum test

- $\delta\omega_S$ - gyroscope reading standard uncertainty

- $\delta\omega_C$ - cross axis interference

- $\delta\omega_B$ - gyroscope B-type uncertainty

Table 6: Uncertainty budget for angular speed

| Quantity | Estimate | Standard Uncertainty | Probability Distribution | Sensitivity Coefficient | Uncertainty Contribution in deg / s |
|---|---|---|---|---|---|
| $\delta\omega_T$ | 80 units | 20.7 units | rectangular | $\frac{360}{798\cdot 2\cdot \pi}$ | 1.5 |
| $\sigma\omega_R$ | 0 | 0.1 deg/s | normal | 1 | 0.1 |
| $u\omega_O$ | 0 | $5.1\cdot 10^{-4}$ deg/s | normal | 1 | $5.1\cdot 10^{-4}$ |
| $\sigma\omega_V$ | 0 | 3.3 units | rectangular | $\frac{360}{798\cdot 2\cdot \pi}$ | 0.2 |
| $\sigma\omega_S$ | 0 | 0.9 deg/s | normal | 1 | 0.9 |
| $\sigma\omega_B$ | 0 | 0.02 deg/s | uniform | 1 | 0.02 |
| $\delta\omega_C$ | 0 | 106.2 units | rectangular | $\frac{360}{798\cdot 2\cdot \pi}$ | 7.6 |
| Standard uncertainty 68 % confidence level, coverage factor k = 1 | | | | | 7.8 deg/s |
| Expanded uncertainty 95 % confidence level, coverage factor k = 2 | | | | | 15.6 deg/s |

# 4 Testing and Calibrating of Magnetometer

## 4.1 Calibration of Angular Displacement

Measurement of magnetic field orientation is performed to find magnetometer calibration curve, estimated angle uncertainty and combined repetitiveness uncertainty and measurement standard deviation. In the test ADCS , CDHS and debug boards are used. To increase similarity to orbital conditions, Earth magnetic field is used as reference in the measurement of magnetic vector orientation. In order to minimize magnetic interference number of electronic devices is limited. Longer wires are used to put more distance between computer and system under test.

Test is performed on table where 90 deg angles are drawn with the ruler and protractor. In the test at least 40 measurements at 5 cycles are taken over 360 deg with the steps of 90 deg. Rotations are made in x and y plain. Test purpose is to find calibration function for relative angular displacement around z-axis to improve estimation of E-sail effect. Magnetic vector rotation calibration curve is presented in Figure 15. In Equation 14 magnetometer calibration curve is estimated.

If $\alpha_m$ is measured angular displacement around z-axis in deg, then accurate angular displacement $\alpha$ in deg is

$$\alpha = 1.0 \cdot \alpha_m + 0.3 \tag{14}$$

Estimated angle uncertainty can be estimated with protractor B-type uncertainty. In the test protractor with a resolution of 1 deg is used to mark the angles

is calculated in Equation 15 , which is used to measure angles between lines drawn on the table.

$$\delta\alpha_P = \frac{1 \deg}{\sqrt{12}} = 0.3 \deg \tag{15}$$

To estimate standard deviation of measured angle 40 measurements averaged x-, y-and z-axes are found. Also standard deviation of each axis is calculated. Then standard uncertainty of all the sets with same angle for each axes is calculated. In Equation 16 standard uncertainty is calculated for x-axis. In Equation 17 standard uncertainty vector form x-, y-and z-axes components is made. In Equations 18, 19 the calculation of averaged results vector is described. Finally in Equation 20, 21 measured angle standard uncertainty is calculated in deg. The largest uncertainty is presented.
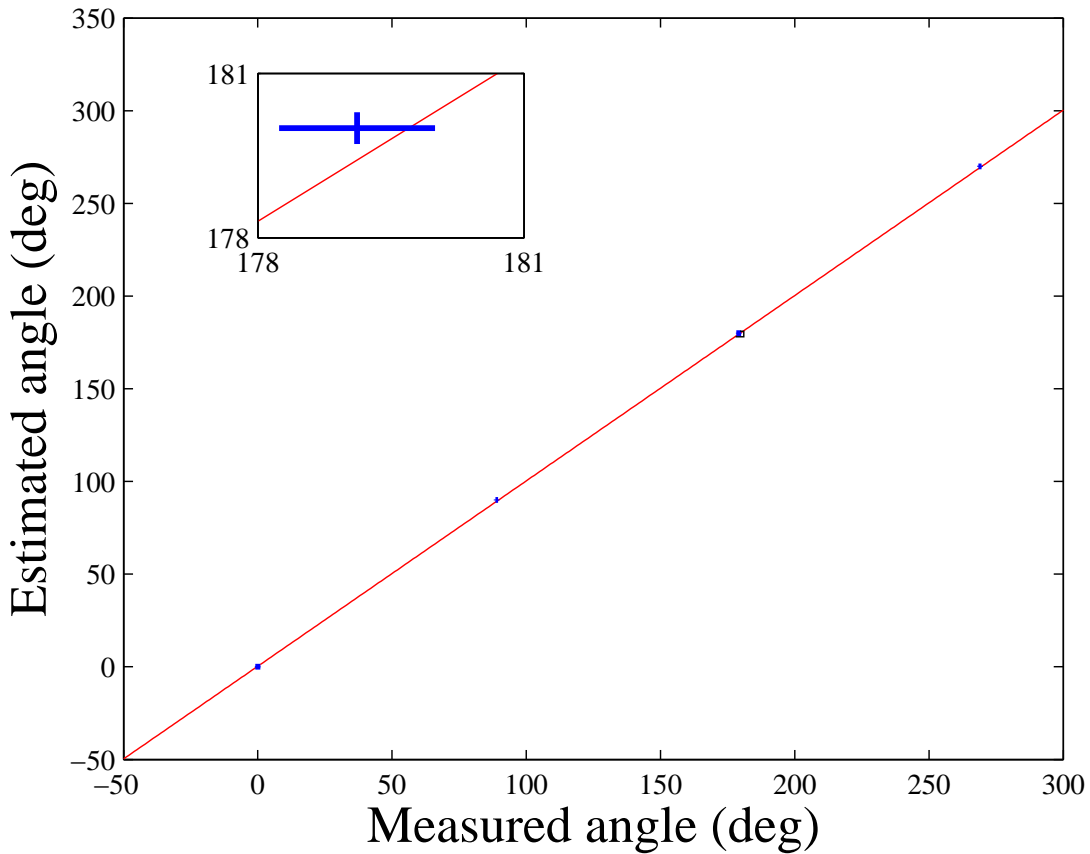
Figure 15: Magnetic field rotation calibration curve. Red line describes the calibration curve of angular rotation, blue lines describe measured angle and estimated angle uncertainties. Inline frame is zoomed in sections in section showing the dispersion of single point measurement series.

If $v_{A,\,x,\,n}$ are one axis averaged measurement sets at one angle, $v_{A,\,x}$ is average over all one axis averaged measurements sets at one angle, $v_A$ is vector made of x-, y-and z-axes averaged results at one speed, $std_{x,\,1}, std_{x,\,2} \cdots$ are one axis standard deviations, $u_{A,\,x}$ is one axes standard uncertainty, $u_A$ i vector made of x-, y- and z-axes standard uncertainties and $\Theta(v_A, v_A + u_A)$

describes the angle between two vectors , then measured angle uncertainty $\alpha_S$ is

$$u_{A,\,x} = \frac{\sqrt{std_{x,\,1}^2 + std_{x,\,2}^2 + std_{x,\,3}^2 + std_{x,\,4}^2 + std_{x,\,5}^2}}{\sqrt{5}} \text{ units} \tag{16}$$

$$u_A = (u_{A,\,x} \text{ units},\ u_{A,\,y} \text{ units},\ u_{A,\,z} \text{ units}) \tag{17}$$

$$v_{A,\,x} = \frac{1}{n} \sum_{i=1}^{n} v_{A,\,x,\,n} \text{ units} \tag{18}$$

$$v_A = (v_{A,\,x} \text{ units},\ v_{A,\,y} \text{ units},\ v_{A,\,z} \text{ units}) \tag{19}$$

$$\alpha_S = \Theta(v_A, v_A + u_A) \text{ deg} \tag{20}$$

$$\alpha_S = 1.0 \text{ deg} \tag{21}$$

Variance of same angle measurement sets is smaller than measured angle uncertainty therefore no further uncertainty analysis is needed.

## 4.2 Effect of Temperature

Temperature test is performed to determine temperature affect on magnetometer results. Five cycles of magnetic vector measurements are made from -10 °C to 35 °C with the steps of 10 °C. During the test magnetometers stood still. In the test temperature chamber Weiss WKL 64 and commeter (combined thermometer, hygrometer, barometer) D4141 are used.

Integrated ADCS, CDHS and debug board are put inside of temperature chamber on a non magnetic surface. Measurement probe of commeter is put as close to ADCS as possible, to increase accuracy of temperature measurements. Temperature chamber is shut down during the measurement acquisition to reduce magnetic noise. In Figure 16 correlation between temperature change in °C and magnetic field magnitude in units is shown. Estimation of temperature caused magnetic vector uncertainty in deg is in Equation 22. The estimation of magnetic field vector uncertainty due to temperature is chosen to describe uncertainty.

Assuming that $\Theta$ is angle between $v_{max}$ magnetic vector measurement at 35 °C and $v_{min}$ magnetic vector measurement at -10 °C, then $\delta\alpha_T$ magnetic vector angular uncertainty due to temperature is

$$\delta\alpha_T = \frac{\theta(v_{max}, v_{min}) \text{ deg}}{\sqrt{12}}$$
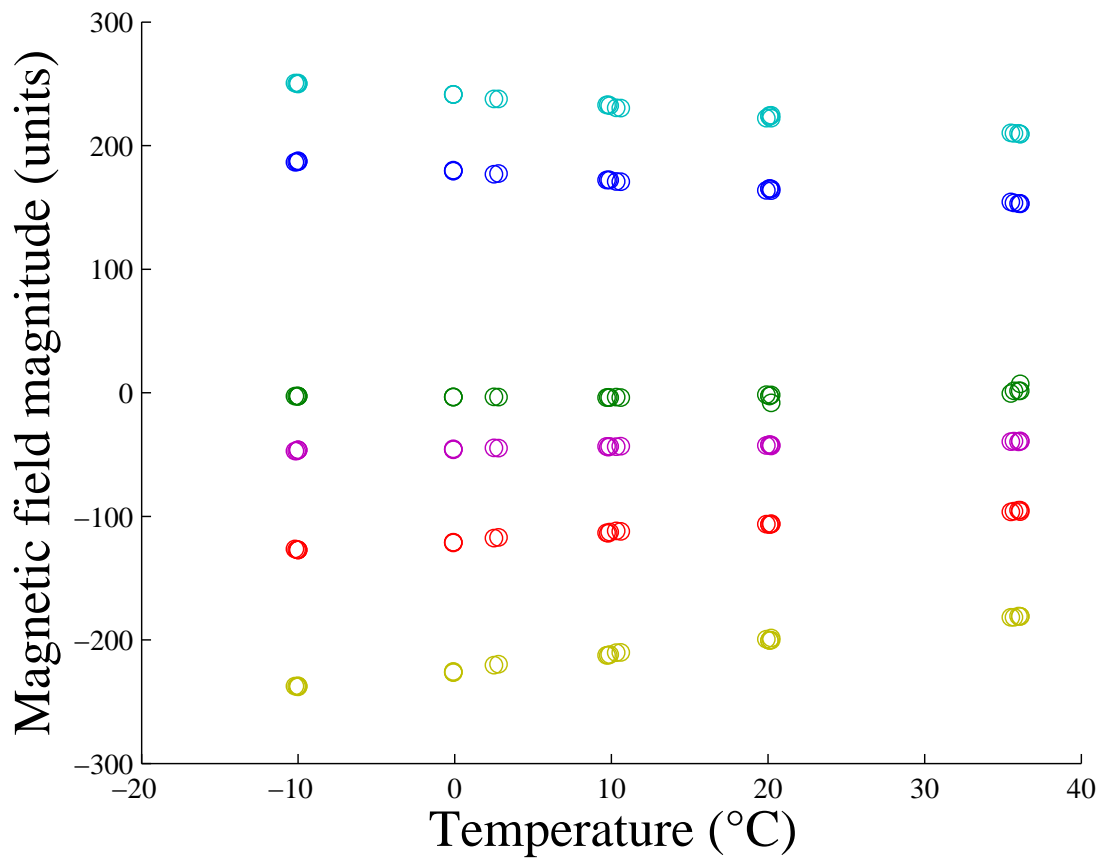
$$= 1.4 \text{ deg} \tag{22}$$

Figure 16: Relationship between temperature and magnetometer readings. Blue - magnetometer 1 x-axis, red - magnetometer 1 y-axis, green - magnetometer 1 z-axis, light blue - magnetometer 2 x-axis, yellow - magnetometer 2 y-axis, purple - magnetometer 2 z-axis

## 4.3 Uncertainty Budget of Magnetic Field Vector Angle

This budget describes accuracy of relative angular change measurement of magnetic field vector.

- $\delta\alpha_S$ - measured angle standard uncertainty

- $\delta\alpha_T$ - uncertainty of temperature effects

- $\delta\alpha_P$ - protractor uncertainty

Table 7: Uncertainty budget of magnetic field vector angle

| Quantity | Estimate | Standard Uncertainty | Probability Distribution | Sensitivity Coefficient | Uncertainty Contribution in deg |
|---|---|---|---|---|---|
| $\delta\alpha_S$ | 0 | 0.8 deg | normal | 1 | 0.8 |
| $\delta\alpha_T$ | 0 | 1.4 deg | rectangular | 1 | 1.4 |
| $\delta\alpha_P$ | 0 | 0.3 deg | uniform | 1 | 0.3 |
| Standard uncertainty 68 % confidence level, coverage factor k = 1 | | | | | 1.6 deg |
| Expanded uncertainty 95 % confidence level, coverage factor k = 2 | | | | | 3.2 deg |

# 5   Discussion and Conclusions

Attitude determination and control system main board was designed. The resulting hardware (Figure 17) with dimensions of 92 mm $\times$ 94 mm $\times$ 5 mm was developed. Module mass with three coils is 90 g shown in appendix B which meets the requirements.
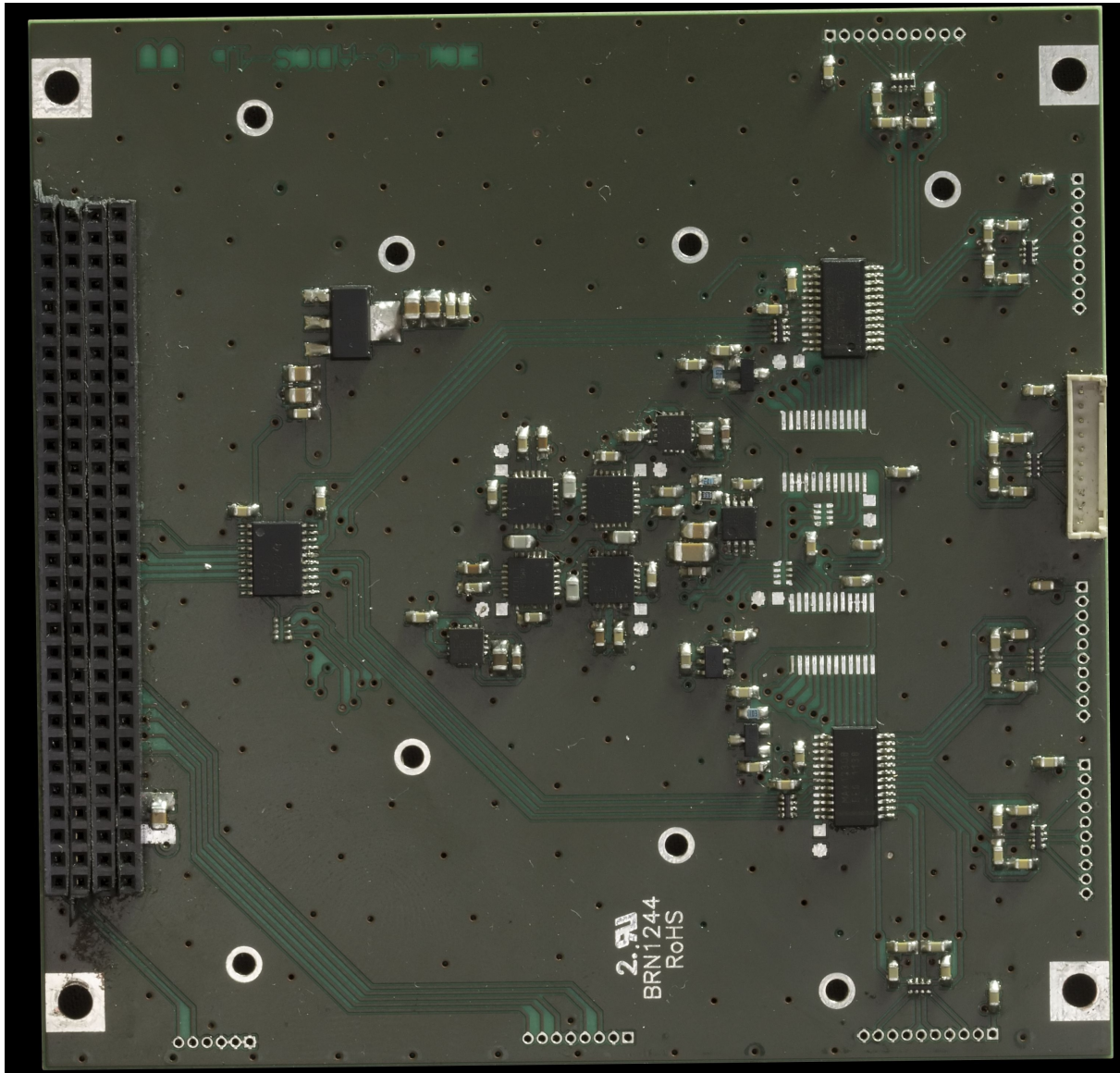


Figure 17: ADCS main board

Power consumption tests show that the power consumption requirements were met with average power consumption of 262 mW. In stand by mode ADCS board consumes 100 mW. The stand by power consumption could be lowered by adding switches to turn off devices that do not have stand by mode. Switches would also add possibility to restart devices without restarting whole ADCS.

Temperature tests confirm, that ADCS board is operating reliably in temperature range of -10 °C to 35 °C which is estimated temperature range. In very high and low temperatures I$^2$C errors can ruin single readings, however these errors can be filtered out by software, thus very high and low temperatures operation can still be carried out.

A robust system which can withstand space conditions for one year, is guaranteed by using components with extended temperature range and duplicating components in critical points. Protection from latch up is provided by EPS, which has sensors to detect power peaks and shut down ADCS, if power measurements are out of boundaries. Robustness of sun vector measurement was reduced in late phase due to the incompatible ADCS and CDHS devices on 5 V tolerant SPI line. To solve the problem in future projects, level converter has to be used.

To increase measurement accuracy calibration of magnetometer and gyroscope was performed. Calibration curve and uncertainty budget of gyroscope angular speed measurement were found. Expanded uncertainty of angular speed measurement was found to be 15.6 deg/s with confidence level of 95%. Most of this uncertainty comes from cross axis influence. Main reasons for high cross axis influence might be the low quality of self build rotation bench. Expanded uncertainty of magnetic field vector angle was found to be 3.2 deg with confidence level of 95%. The biggest uncertainty component of magnetic field vector is uncertainty of temperature effect.

Uncertainties of angular speed measurement and magnetic field vector angle are inputs for Kalman filter. Averaging over multiple measurements and filtering out errors with software, would further increase accuracy of the measurements. Based on tests, designed hardware is able to fulfill its operational tasks on orbit.

Success of meeting the requirement for relative angular speed measurement accuracy to estimate E-sail effect, will be determined during mission.

# 6  Summary

Space qualified ADCS main board for the Estonian first satellite ESTCube-1 was developed in this thesis. Hardware that meets the requirements described in phase B ADCS document was developed, integrated. Developed system of ADCS is custom made to fulfill needs of ESTCube-1 mission.

Testing and calibrating of magnetometer and gyroscope was performed. Calibration functions to decrease measurement uncertainty where calculated. Uncertainties of angular speed measurement and magnetic field vector angle inputs for Kalman filter were found.

Preliminary ESTCube-1 results show ADCS sensors are functioning in orbit.

# 7  Acknowledgments

# 8 Kokkuvõte

Käesoleva töö käigus arendati välja Eesti esimese satelliidi ESTCube-1 asendi määramise ja juhtimise süsteemi kosmosesse minev põhiplaat, integreeriti käsu- ja andmehaldussüsteemiga ning viidi läbi magnetomeetri ning güroskoobi kalibratsiooni ja määramatuse leidmise teste.

Töökindla plaadi disainimise käigus uuriti erinevaid komponente ja nende positiivseid ning negatiivseid külgi. Lisaks kirjeldati disaini seisukohast olulisi parameetreid ning lõpetuseks analüüsiti vigu, mida järgmistes projektides tuleb vältida.

Magnetomeetri ja güroskoobi kalibreerimine ja testimine viidi läbi eesmärgiga suurendada mõõtmiste täpsust. Testimise käigus leiti magnetomeetri magnet välja nurga määramise ja güroskoobi nurkkiiruse määramatused . Määramatused on sisendid asendi määramise ja juhtimise süsteemi kontroll algoritmile,s.t Kalman filtrile.

Esimesed ESTCube-1 tulemused kinnitavad, et satelliidi asendi määramise ja juhtimise süsteemi sensorid töötavad edukalt.

# References

[1] California Polytechnic State University The Cubsat Program. CubSat Design Specification Rev. 12, 2009.

[2] Boeing successfully completes cubesat mission to advance nano-satellite technology, http://www.boeing.com/news/releases/2007/q3/070816a_nr.html, (accessed 20th of may 2013), 2007.

[3] Masat-1 homepage, http://cubesat.bme.hu/en/ (accessed 20th of may 2013).

[4] Estcube-1 homepage, www.estcube.eu, (accessed 20th of may 2013).

[5] J. Polkko S. Merikallio P. Salminen E. Haeggstrom H. Seppanen R. Kurppa J. Ukkonen S. Kiprich G. Thornell H. Kratz L. Richter O. Kromer R. Rosta M. Noorma J. Envall S. Latt G. Mengali A. A. Quarta H. Koivisto O. Tarvainen T. Kalvas J. Kauppinen A. Nuottajarvi A. Obraztsov P. Janhunen, P. K. Toivanen. Invited article: Electric solar wind sail: Toward test missions. *Review of Scientific Instruments*, 81:111301–1, 2010.

[6] R. Valner. Characterisation of Custom Built Sun Sensor for ESTCube-1, Bachelor's thesis, University of Tartu, 2013.

[7] Jens Giesselmann. Development of an active magnetic attitude determination and control system for picosatellites on highly inclined circular low earth orbits. Master's thesis, RMIT University, 2006.

[8] B.Dachwald J.J.Miau J.C.Juang A. Scholz, W.Ley. Flight results of the compass-1 picosatellite mission. *Acta Astronautica*, 67:1289–1298, 2010.

[9] S. Inagawa Y. Miura K. Omagari N. Miyashita S. Matunaga T. Toizumi J. Kataoka N. Kawai H. Ashida, K. Fujihashi. Design of Tokyo Tech nano-satellite Cute-1.7 + APD II and its operation. *Acta Astronautica*, 66:1412–1424, 2010.

[10] S.J. Kim S.J. Kang Y. K. Chang, B.H. Lee. HAUSAT-2 nanosatellite ADCS performance analysis and commissioning. In *Proceedings of the 2nd International Conference on Recent Advances in Space Technologies*, pages 180–184, June 2005.

[11] S.-J. Kim Y.-K. Chang, B.-H. Lee. Analysis of the Hausat-2 Attitude Controll With a Pitch Bias Momentum System. In *5th IAA Symposium*, Berlin, Germany, April 4-8 2005.

[12] Stuart Eagleson Daniel D. Kekez Amee Shah Robert E. Zee Karan Sarda, Cordell Grant. Canadian advanced nanospace experiment 2 orbit operations: One year of pushing the nanosatellite performance envelope. Technical report, Space Flight Laboratory ,University of Toronto Institute for Aerospace Studies, 2010.

[13] University of würzburg experimentalsatellit-1 homepage , http://www.eoportal.org/directory/presuwe1universittwrzburgsexperimentalsatellit1.html , (accessed 20th of may 2013).

[14] Honeywell. *Three-Axis Digital Compass IC HMC5843, http://www51.honeywell.com/aero/common/documents/myaerospacecatalog-documents/Defense_Brochures-documents/HMC5843.pdf (accessed 15th of May).*

[15] Honeywell. *Three-Axis Digital Compass IC HMC5883L, http://www51.honeywell.com/aero/common/documents/myaerospacecatalog-documents/Defense_Brochures-documents/HMC5883L_3-Axis_Digital_Compass_IC.pdf (accessed 10th of May).*

[16] InvenSense Inc. *ITG-3200 Product Specification; www.invensense.com.* InvenSense Inc., 1197 Borregas Ave, Sunnyvale, CA 94089 U.S.A., 1.4 edition, 2010 03/30/2010.

[17] V. Apostolyuk. *Theory and design of micromechanical vibratory gyroscopes MEMS/NEMS Handbook.* Springer, 2006.

[18] Mauro Marchi Simone Sassolini Lorenzo Baldo, Marco Del Sarto. Mems-type high-sensitivity inertial sensor and manufacturing process thereof ep 1624284 a1, 2006.

[19] Maxim integrated products. *12-Bit 300 ksps ADCs with FIFO, Temp Sensor, Internal Reference, http://datasheets.maximintegrated.com/en/ds/MAX1226-MAX1230.pdf* , 5 edition, December 2010.

[20] Jesper A. Larsen Kasper Vinther, Kasper F. Jensen and Rafael Wisniewski. Inexpensive CubeSat Attitude Estimation Using Quaternions and Uncented Kalman Filtering. *Automatic Controll in Aerospace*, (ISSN 1974-5168), March 2011.

[21] Expression of the Uncertainty of Measurement in Calibration, European co-operation for Accreditation, 1999.

[22] Andrew T. Klesh Matthew W. Bennett James W. Cutler John C. Springmann, Alexander J. Sloboda. The attitude determination system of the RAX satellite. *Acta Astronautica*, 75:120–135, 2012.

[23] Sharp Electrionic Components. *GP2S30 - Long Focal Distance Type Photointerrupter with Connector, http://pdf1.alldatasheet.com/datasheet-pdf/view/42849/SHARP/GP2S30.html (accessed 10th of May).*

[24] ROHDE & SCHWARZ. *R&S RTO Digital Oscilloscope, http://www.rohde-schwarz.com/en/product/rto-productstartpage_63493-10790.html (accessed 12th of May)).*

# Appendices

# A Appendix 1 - ESTCube-1 Structure



Solar sensor

Solar panel

Attitude determination and control system (ADCS)

Payload 2: Producing and controling high voltage (PL2)

Antenna (Uplink)

Onboard camera (CAM)

Payload 1: Tether reel motor and electronics (PL1)

Tether endmass

Access port

Frame (STR)

Side panel

Electron cannon

Electromagnet

Command and data handling system (CDHS)

Electrical Solar Wind Sail

Tether reel motor

Electrical power system (EPS)

Communication system (COM)

Antenna (Downlink)

The structure of cubesat ESTCube-1

Figure 18: ESTCube-1 structure

# B  Appendix 2 - Mass budget



Figure 19: ADCS main board

Table 8: Mass budget of ADCS

| Device | Mass |
|---|---|
| ADCS main board + 1 coil | 42 g |
| 2 coils | 48 g |
| Sum | 90 g |

Sun sensors mass is not included in this budget.

# C  Appendix 3 - Attitude Determination and Control System Schematics
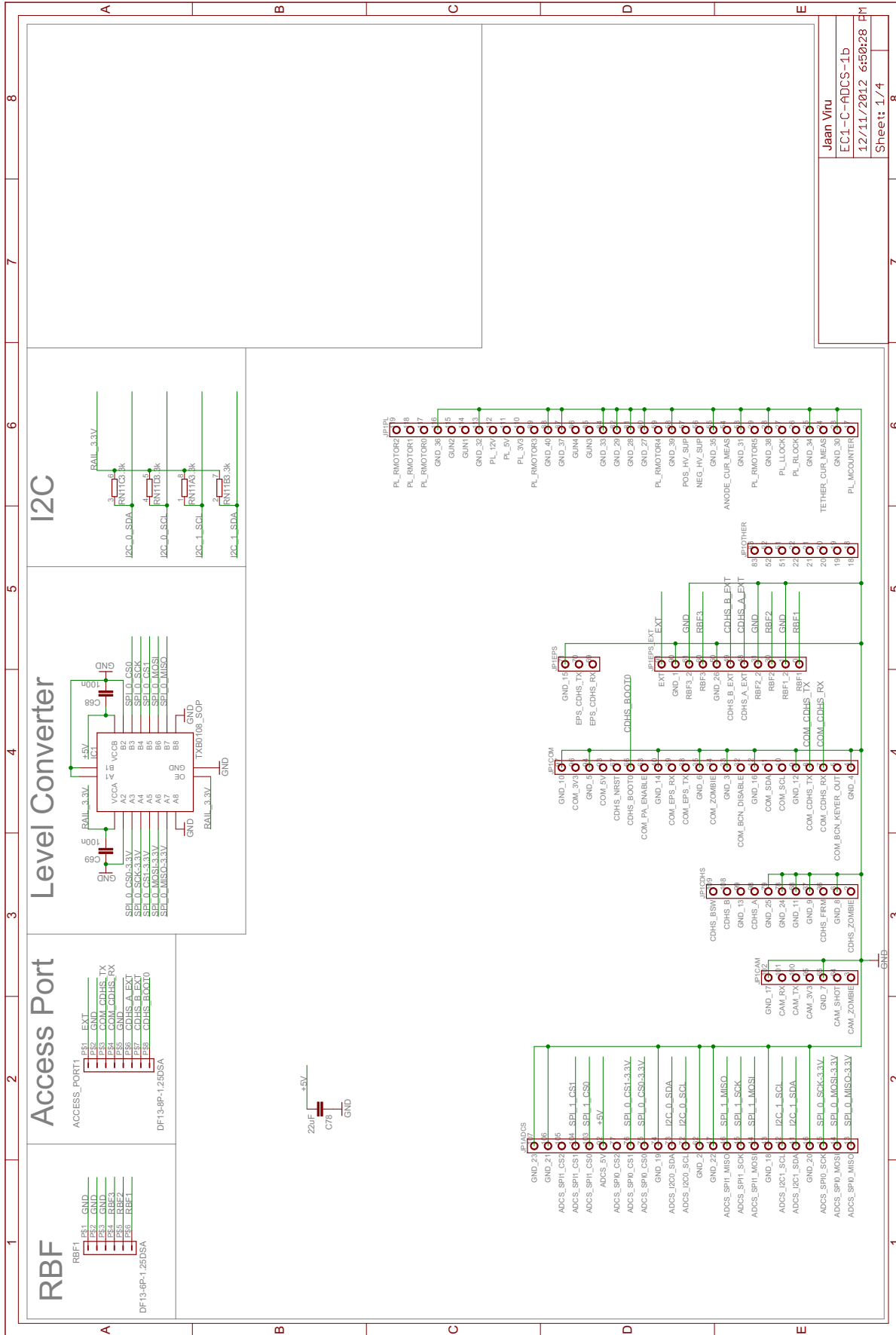
Figure 20: ADCS schematics
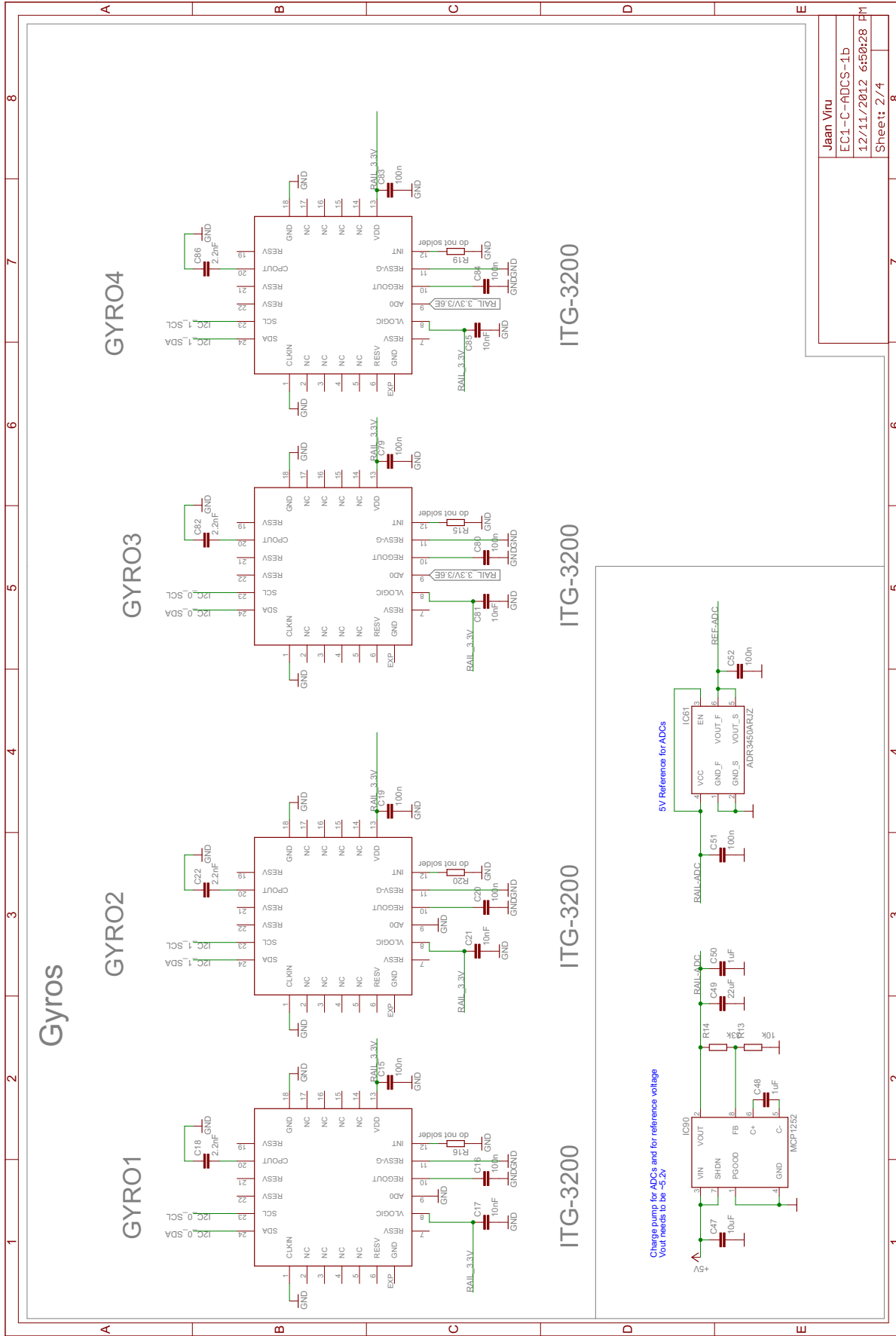
Figure 21: ADCS schematics
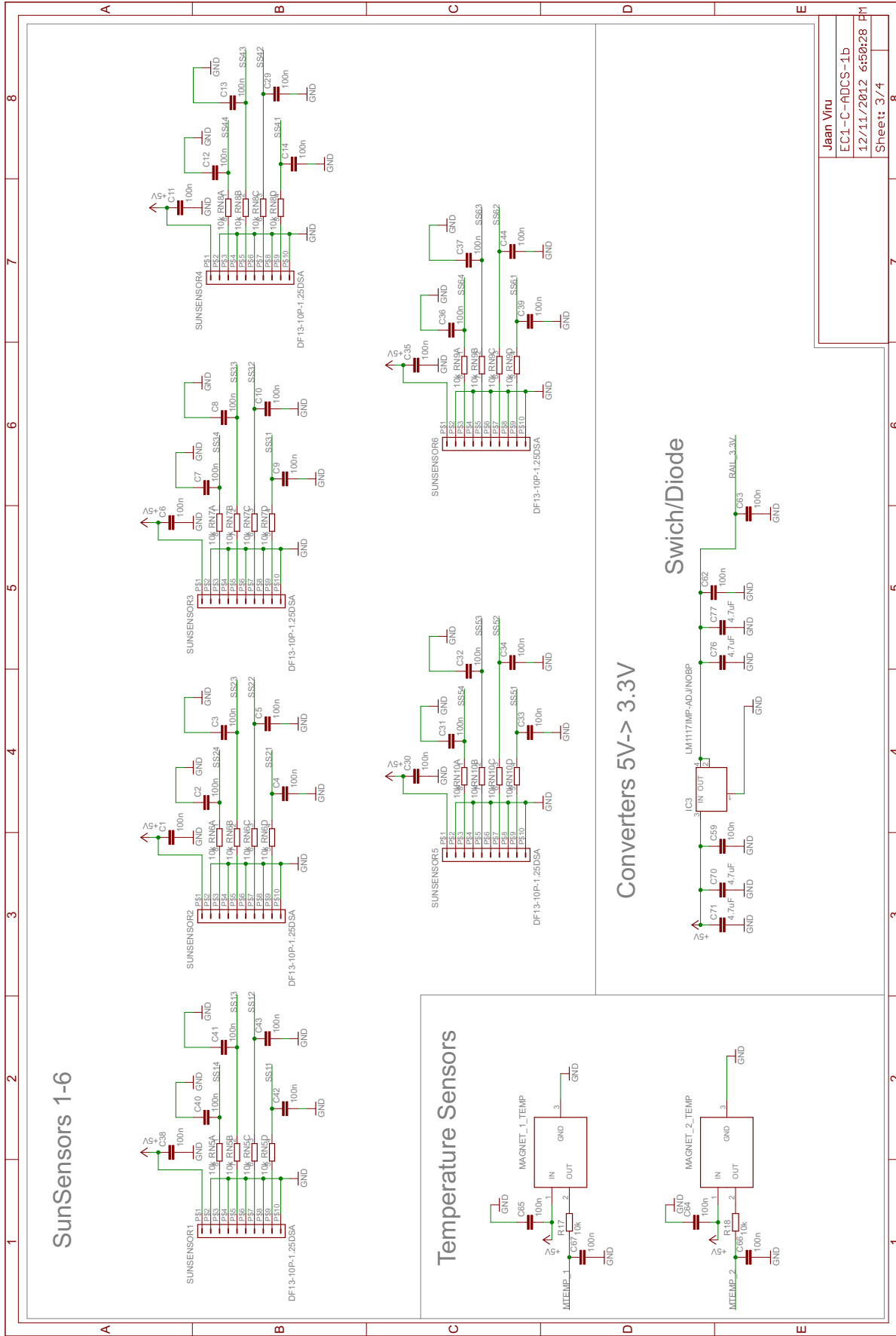
Figure 22: ADCS schematics
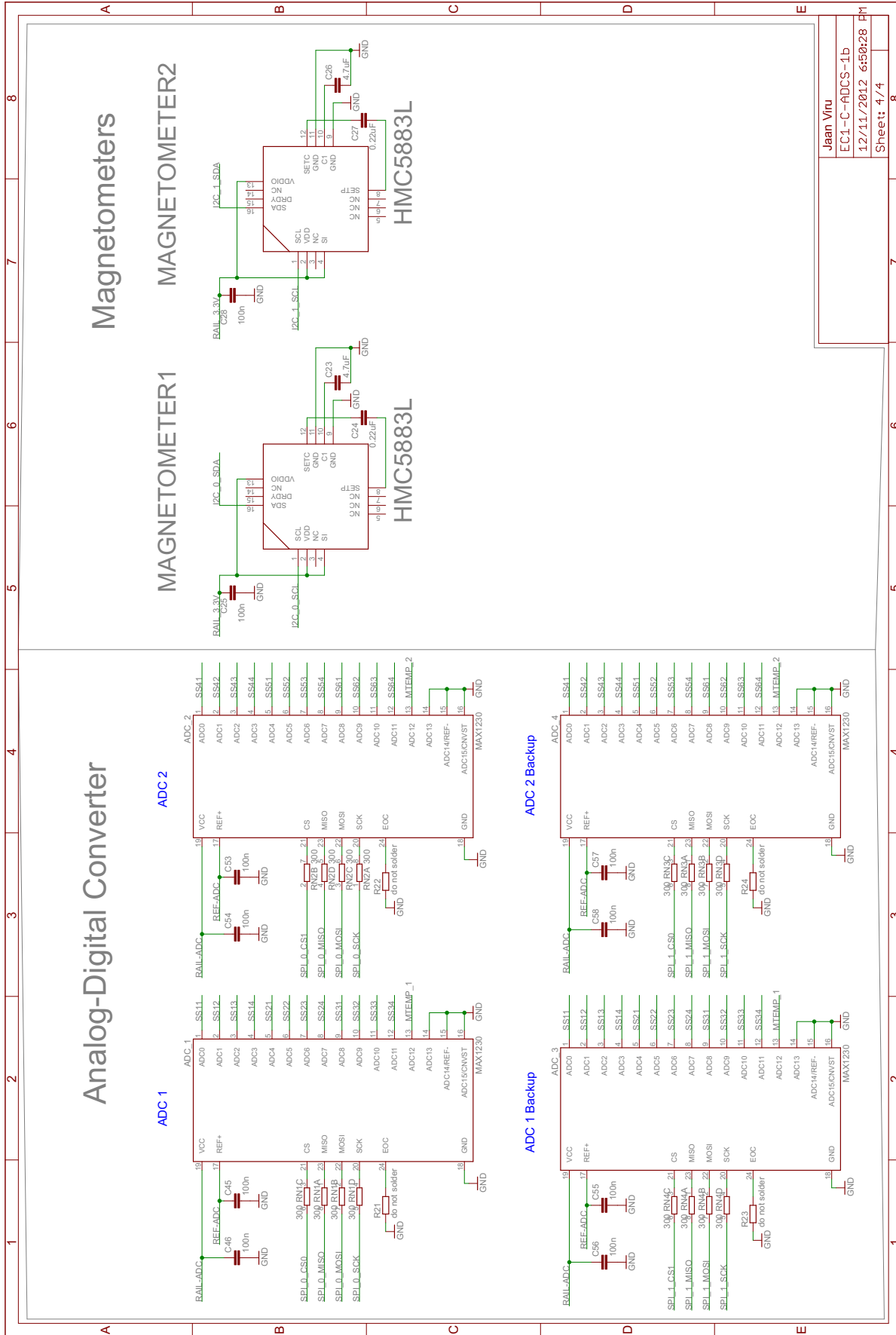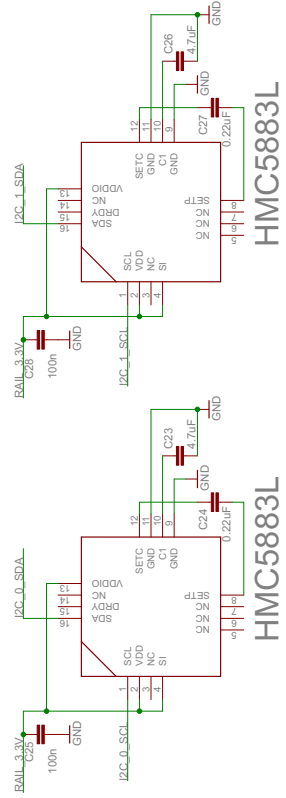
41
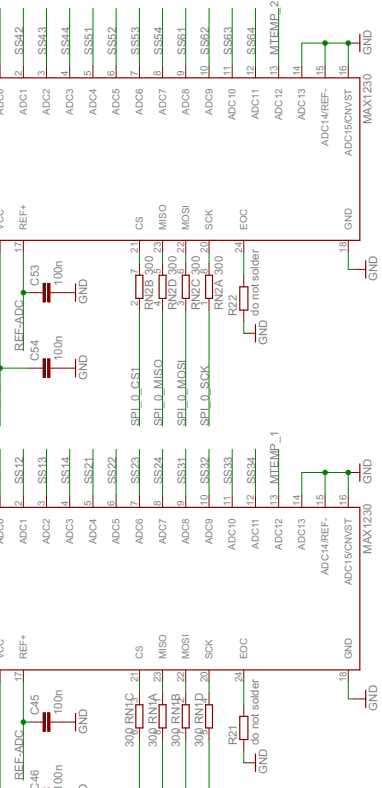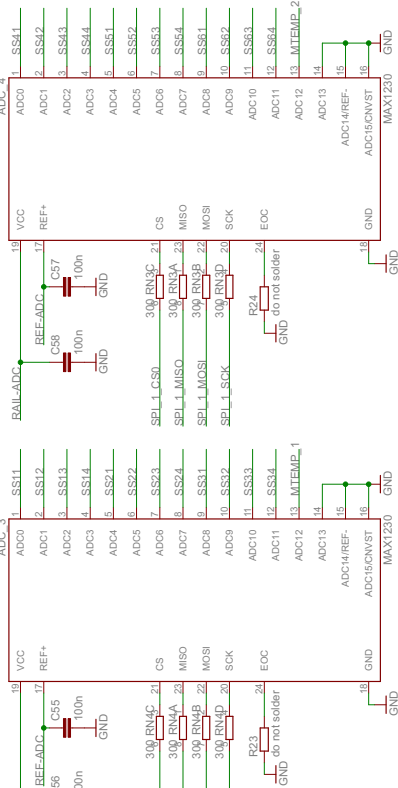
Figure 23: ADCS schematics

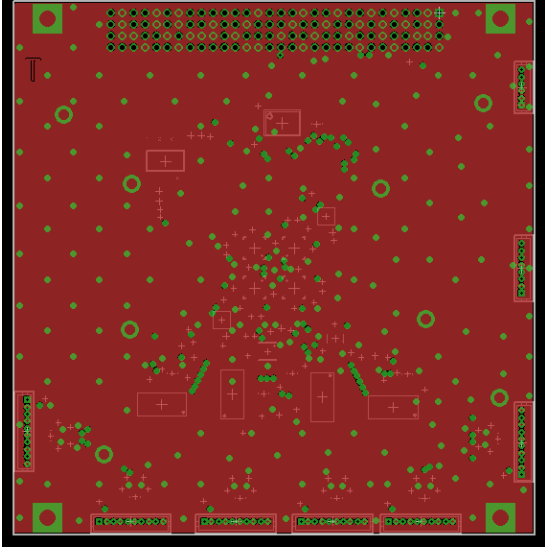# D   Appendix 4 - Attitude Determination and Control System Printed Circuit Board Layout



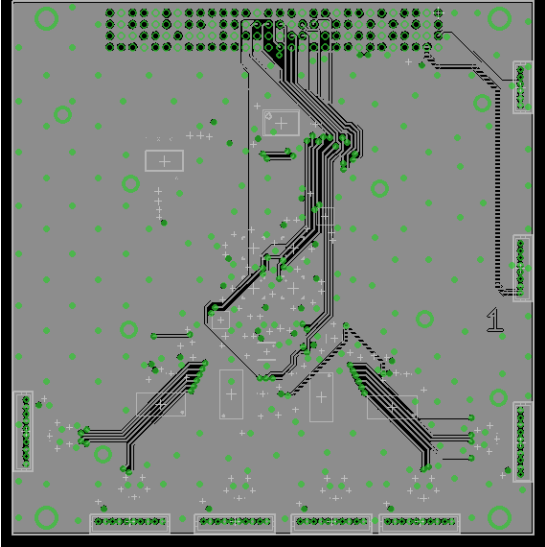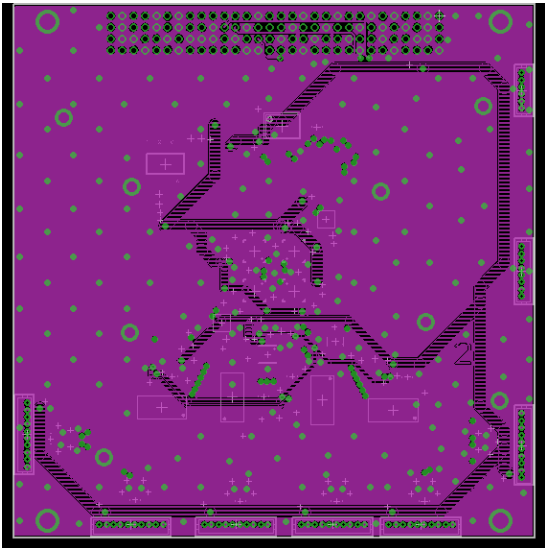Figure 24: Top layer of ADCS PCB , 1



Figure 25: Middle layer of PCB, 2



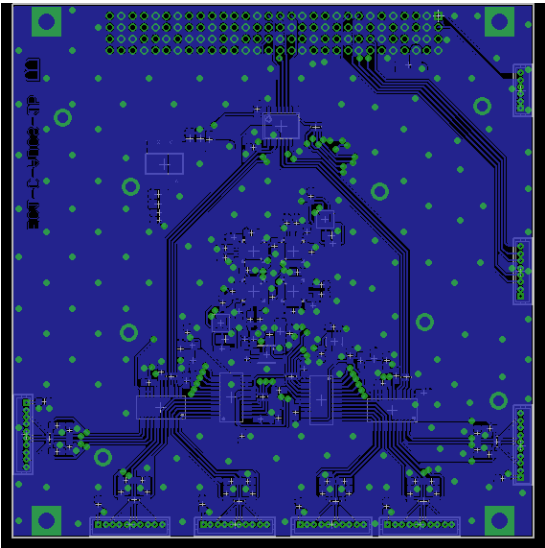Figure 26: Top layer of ADCS PCB , 3



Figure 27: Bottom layer of PCB, 4

**Non-exclusive licence to reproduce thesis and make thesis public**

I,  Jaan Viru  (date of birth: 03.07.1990),

1.   herewith grant the University of Tartu a free permit (non-exclusive licence) to:

1.1. reproduce, for the purpose of preservation and making available to the public, including for addition to the DSpace digital archives until expiry of the term of validity of the copyright, and

1.2. make available to the public via the web environment of the University of Tartu, including via the DSpace digital archives until expiry of the term of validity of the copyright,

Design and Testing of Attitude Determination Sensors for ESTCube-1,
(title of thesis)

supervised by M.Sc. Andris Slavinskis and M.Sc. Riho Vendt,
(supervisor's name)

2. I am aware of the fact that the author retains these rights.

3. I certify that granting the non-exclusive licence does not infringe the intellectual property rights or rights arising from the Personal Data Protection Act.

Tartu, **31.05.2013**